Article

Not peer-reviewed version

Three-Channel Rayleigh Lidar System Signal Retrievals

Satyaki Das , Richard Collins * , Jintai Li

Posted Date: 2 March 2026

doi: 10.20944/preprints202603.0047.v1

Keywords: ayleigh density and temperature lidar; instrumental bias; pulse pile-up

 doi:10.20944/preprints202603.0047.v1

Article

Three-Channel Rayleigh Lidar System Signal Retrievals

Satyaki Das, Richard Collins * and Jintai Li

Geophysical Institute, University of Alaska, Fairbanks

* Correspondence: rlcollins@alaska.edu

Abstract

A single channel Rayleigh Density Temperature Lidar (RDTL) with a receiver telescope of 85 cm diameter was installed at Poker Flat Research Range (PFRR), Chatanika, Alaska (65°N, 213°E) in November 1997. To increase the incoming signal count the receiver diameter was increased to 1 m in 2016. In order to prevent damage of the photomultiplier tube due to the high incoming signal counts, the RDTL receiver system was modified to a three-channel system. However, temperature calculations from the individual channel retrieval showed a mismatch between them and this created a problem in combining the signal counts from the three channels into one to achieve higher confidence in the data. In this study, a correction procedure has been developed and deployed to the signal counting statistics of the RDTL to eliminate instrumental biases and get 100% agreement in temperatures between the three channels.

Keywords: rayleigh density and temperature lidar; instrumental bias; pulse pile-up

1. Introduction

The Rayleigh Density Temperature Lidar system (RDTL) was installed at Poker Flat Research Range (PFRR), Chatanika, Alaska (65°N, 213°E) in November 1997. The lidar was initially developed as part of the Alaska project, a collaboration between the National Institute of Information and Communications technology (NICT) and Geophysical Institute of the University of Alaska, Fairbanks (GI-UAF) (Mizutani et al., 2000). The Rayleigh lidar, which initially had one channel receiver system (Cutler et al., 2001; Collins et al., 2003) was modified to a two-channel system in 2015 (Triplet et al., 2018) and a three-channel system in 2017 (Alspach, 2020). The three-channel system was designed to increase the overall lidar signal by increasing the aperture of the receiver telescope (from 0.6 m diameter to 1.03 m diameter) while avoiding distortion of the signal that would result from collecting all the back scattered light if a single-channel receiver with a single detector was used. When a large optical signal is incident on the photocathode of the photomultiplier tube (PMT), the PMT draws a large current from its power supply and hence the terminal voltage of the power supply decreases due to voltage drop in the output impedance of the supply. Thus, the bias voltage of the PMT is reduced and the gain of the PMT is reduced. While the voltage recovers as the signal decreases, the recovery depends on the resistive-capacitive time constants of the PMT power supply, and so the lidar signal is distorted as the gain increases in time (and altitude). The splitting of the signal was done using beam splitters and mirrors that directed a fraction of the received light into three separate channels with independent detectors. An initial beam splitter directed ~20% of the received light into the first channel (Channel 1), a second beam splitter directed ~50% of the remaining light (~40% of the total) into the second channel (Channel 2) and a mirror directed the remaining light (~40% of total) into the third channel (Channel 3) (Figure 1). The initial retrieval method was developed where the Channel 1 signal was used at lower altitudes and the Channel 2 signal used at upper altitudes, and the signals were connected at altitudes where the vertical gradients of the signals were closest in value (Alspach, 2020). However, the method did not systematically correct the independent channels before combining them. We now present a comprehensive retrieval method where we correct the

 doi:10.20944/preprints202603.0047.v1

channels for pulse pile-up, the gain-switching response of the detectors, and the relative fidelity of the signals in each channel. We assume that the lowest amplitude signal (Channel 1) has the best fidelity, and most accurately represents the atmospheric density profile.

2. Instrument

The RDTL has three major subsystems – a transmitter, a receiver system, and a data acquisition system (Figure 1). The transmitter is composed of a Nd:YAG laser, a laser pulse detector, and a beam steering mirror. The laser operates at 532 nm wavelength and operates at 20 pulses-per-second (pps). The laser beam is then directed vertically into the sky by the beam steering mirror. The receiver is composed of a telescope, pinhole, collimation lens, beam splitters and mirrors, interference filters, focusing lenses and PMTs. The backscattered light is received by a 1.04 m diameter telescope. A pinhole at the telescope focus determines the receiver field-of-view which is set at 0.5 mrad or 1 mrad. The light is then collimated with a single collimating lens. The collimated light is then split into three channels using beam-splitters. Each channel consists of an interference filter, photomultiplier tube, preamplifier, and high-speed counter. Channel 1 receives 20% of the received light, while Channels 2 and 3 receive 40% of the light. The interference filters are identical with a bandwidth of 0.3 nm and reduce the signal due to the background skylight. The PMTs convert the light into an electronic signal with a quantum efficiency of ~20%, where 5 photons will yield 1 electronic pulse on average. The PMT output signal composed of a sequence of negative going pulses each associated with each photon of light. The electronic signal is then amplified by the pre-amplifier and sent to the data acquisition system. The data acquisition system consists of a high-speed counter called a multi-channel scaler and a computer. The multi-channel scaler (MCS) counts the pulses of the amplified PMT signal in time in a process called photon counting. The MCS uses a threshold to discriminate between low amplitude thermal pulses generated in the PMT (the dark counts) and the higher amplitude pulses generated from the optical signal from the telescope (the signal counts). The MCS counts the signals in 4096 successive 0.32 μs intervals yielding a profile from the ground to 196.6 km at a resolution of 48m. The MCS co-adds the echoes from a given number of laser pulses (500 or 1000) to create a raw lidar profile. A computer initiates the MCS unit, tells it how many echoes to co-add, and then retrieves the raw profile, before initiating the acquisition of the next profile. The specifications of the RDTL are listed in Table 1.

Table 1. RDTL specifications.

Specification	Description
Transmitter	
Laser	Nd:YAG
Model	Continuum Powerlite 8020
Wavelength (λ_L)	532 nm
Repetition rate (R_L)	20 Hz
Pulse energy (E_L)	450-500 mJ
Pulse Width	5-7 ns
Divergence	0.45 mrad
Beam expander	x10
Receiver	
Telescope diameter	1.04 m
Field of view	0.5 mrad
Detector	Photomultiplier tube (Model: Hamamatsu RS3234-1)
Digital Recorder	Multichannel scalar (Model: Stanford Research Systems SR430)

 doi:10.20944/preprints202603.0047.v1

Maximum count rate	100 MHz
Interference bandwidth	0.3 nm
Preamplifier	SR445 300 MHz

In the RDTL the laser is free-running, and the receiver and the data acquisition are synchronized to the laser. When the laser fires the laser pulse detector uses a high-speed photodiode to detect the laser shot and generate a trigger signal. That signal is used to trigger the three MCS units. The laser Q-switch signal, which initiates the laser firing and thus precedes the laser pulse detector signal, triggers the three PMTs so that the gain of the PMT is reduced for an interval after the laser fires, and the detector is not overloaded by the strong echoes from the air close to the ground.

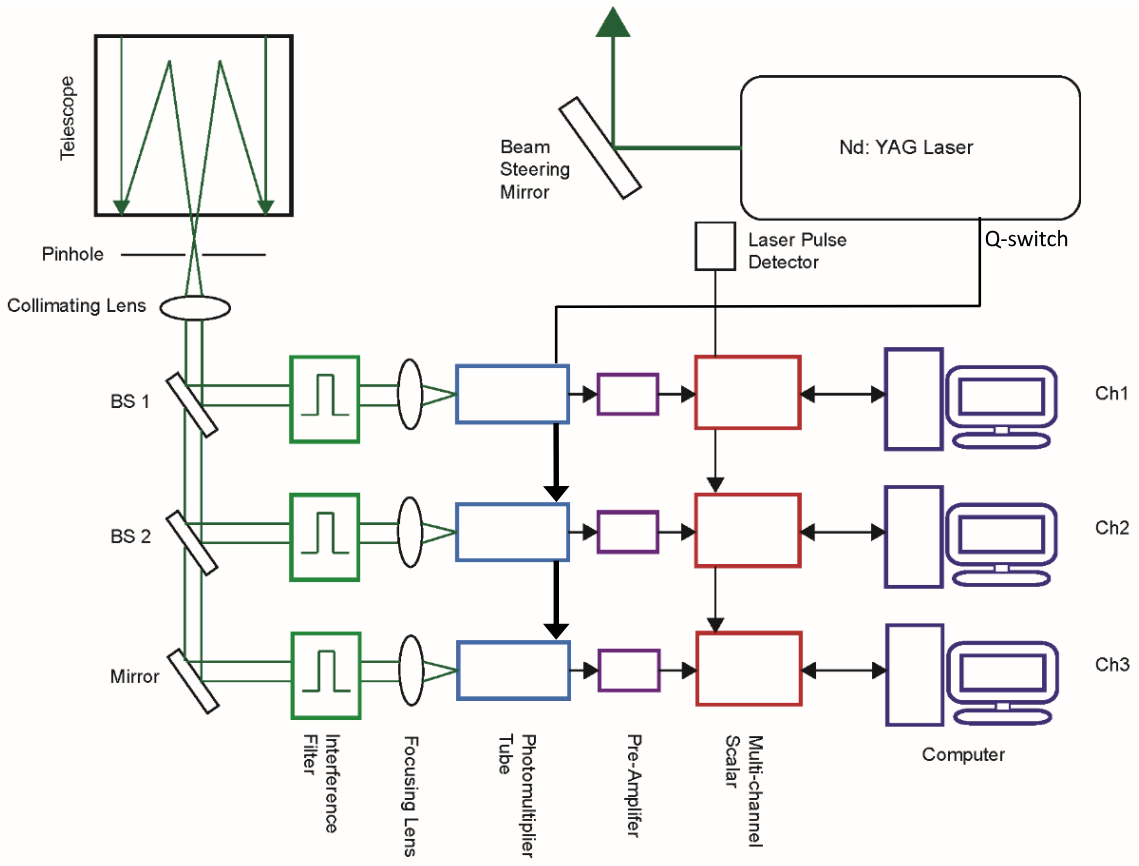

Figure 1. Schematic diagram of the 3-channel Rayleigh Density Temperature Lidar (RDTL) system installed at Poker Flat Research Range, Chatanika, Alaska.

3. The Lidar Equations

The lidar signal is the echo of the laser pulses that are transmitted into the sky. The expected returned lidar signal is proportional to the atmospheric density. The expected total lidar signal from an altitude range (z-Δz/2, z+Δz/2) in a time interval Δt is given by the lidar equation,

$$N_{TOT}(z) = N_s(z) + N_B + N_D \quad (1)$$

where $N_s(z)$ is the lidar signal count proportional to the atmospheric density, N_B is the background skylight count, and N_D is the detector dark count. The detector the lidar count signal N_S, the background skylight count N_B, and the dark count N_D, and are given by,

$$N_B = \eta[H_N R_L \Delta t \pi (\frac{\Delta\theta_R}{2})^2 A_T \Delta\lambda] (\frac{2\Delta z}{c}/\frac{hc}{\lambda}) \quad (2)$$

 doi:10.20944/preprints202603.0047.v1

$$N_D = (C_N R_L \Delta t)\left(\frac{2\Delta z}{c}\right) \quad (3)$$

where η is the receiver efficiency, λ_L is the transmission wavelength (m), T is the atmospheric transmission at λ_L, E_L is the laser energy per pulse (J), R_L is the laser repetition rate (s^{-1}), ρ(z) is the number concentration of scatters at an altitude z (m^3), A_T is the telescope area (m^2), σ_π^R is the effective backscatter cross section at λ_L (5.22×10^{-31} m^2), h is Planck's constant (~6.63×10^{-34} J s), c is the speed of light (3.0×10^8 ms^{-1}), $\Delta\theta_R$ is the field of view of the receiver (0.5 mrad or 1 mrad), H_N is the background sky irradiance (W m^{-2} μm sr), Δλ is the bandwidth of the detector (nm) and C_N is the dark count rate for the detector (s^{-1}). For RDTL, the typical value of Δt is 50 s and of Δz is 48 m.

Figure 2 shows the photon count for the three channel Rayleigh lidar system on October 18-19, 2018. This represents the total signal from 816000 laser pulses, acquired as a series of 816 profiles of 1000 pulses. The data acquisition system acquires 16 raw signal profiles at a time as a set and stores them in an individual data file. On this night 51 sets of profiles were acquired. There is reduced signal below a certain altitude (~25 km Channel 1, ~32 km Channels 2 and 3) as it is suppressed by the electronic gain-switching (or blanking) of the PMT. The high signals from low altitudes close to the receiver would overload the PMTs and distort the lidar signals. Two delay generators generate delays of 150 μs (Channel 1) and 200 μs (for Channels 2 and 3) yielding the blanking altitudes at 25 km for channel 1 and 32 km for channels 2 and 3. Above the blanking altitude the signal decreases exponentially and becomes constant above 100 km where the signal is dominated by the background and dark counts. The differences in the magnitudes of the signals the Channels reflect the beam splitting in the receiver with Channel 1 representing 20% of the total signal, Channel 2 representing 40% of the total signal, and Channel 3 representing 40% of the total signal. The differences from the expected ratios reflect the differences in the transmission of the interference filters in each channel, which are typically 60%. On October 18-19, 2018, the photon counts at 40 km were 1.6e5, 3.8e5 and 4.6e5 for channels 1, 2 and 3 respectively.

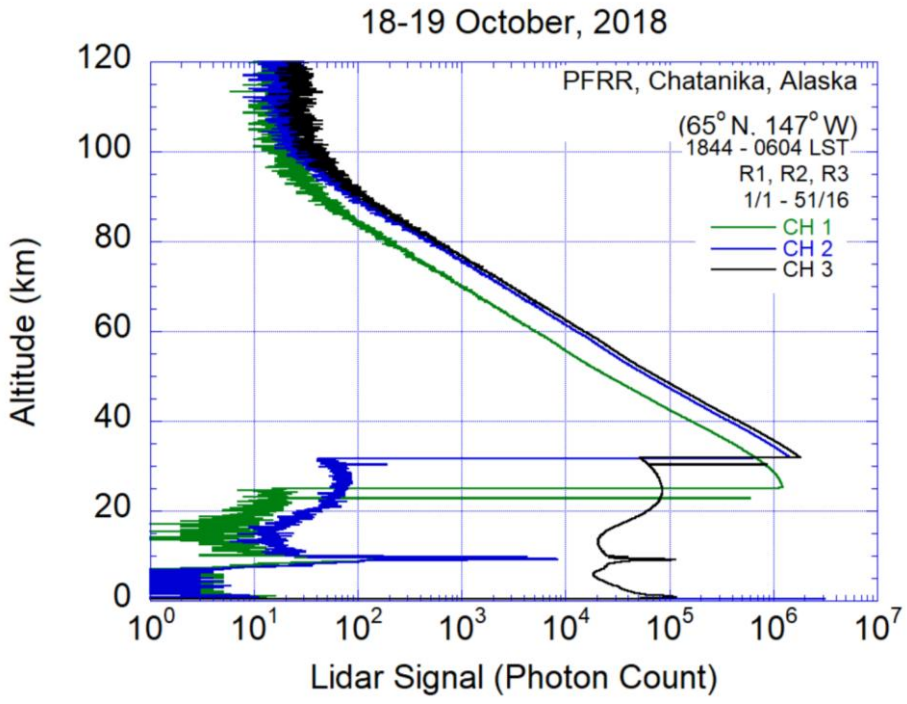

Figure 2. Rayleigh lidar signal plotted as a function of altitude on 18-19 October 2018.

Table 2 presents the RDTL signal counts at different altitudes on October 18-19, 2018. N_T is the total photon count; N_S is the signal count after removing the background and dark counts at 190 km. The combined dark and skylight counts are about 1707, 1839 and 2839 counts for channel 1, 2 and 3 respectively. Typical values for the dark count for RDTL are 43, 17 and 50 counts for channel 1, 2 and

 doi:10.20944/preprints202603.0047.v1

3 respectively (Alspach, 2020). Hence the dark count signal is over an order of magnitude smaller than the skylight count signal.

Table 2. RDTL signals on night of 18-19 October 2018.

Altitude (km)	No. of Bins	N_{TOT}	N_S	ΔN_S
Channel 1				
40 (40-45)	104	1.08E7	1.08E7	3.28E3
60 (60-65)	104	3.67E5	3.65E5	6.04E2
80 (80-85)	105	1.42E4	1.24E4	111
120 (120-125)	104	1689	-18	N/A
190 (190-195)	104	1707	0	0
Channel 2				
40 (40-45)	104	2.55E7	2.53E7	5.03E3
60 (60-65)	104	9.17E5	9.15E5	9.56E2
80 (80-85)	105	3.42E4	3.23E4	179
120 (120-125)	104	1842	3	1.73
190 (190-195)	104	1839	0	0
Channel 3				
40 (40-45)	104	3.12E7	3.12E7	5.58E3
60 (60-65)	104	1.08E6	1.07E6	1.03E2
80 (80-85)	105	4.06E4	3.77E4	194
120 (120-125)	104	2885	46	6.7
190 (190-195)	104	2839	0	0

The counting process is statistical in nature and the Rayleigh lidar signal has a Poisson distribution (Papoulis and Pillai, 2002). The uncertainty in the signal equals the square root of the expected value of the signal. The signal, N_S, is calculated as the total signal (N_{TOT}) minus an estimate of the sum of the background and dark signal ($N_B + N_D$), ($\widetilde{N}_B + \widetilde{N}_D$). As ($N_B + N_D$) does not vary

 doi:10.20944/preprints202603.0047.v1

with altitude, the estimate $(\widetilde{N}_B + \widetilde{N}_D)$ is calculated as an average of the total lidar signal over an altitude range above where N_S is negligible (e.g., > 120 km, over 5 km). The uncertainty in the average is thus much less than the uncertainty in the signal (by a factor of 10 or more for averages over 100 or more range bins) and can be neglected.

$$N_S = N_{TOT} - (\widetilde{N}_B + \widetilde{N}_D) \tag{4}$$

$$\Delta N_S = (\Delta N_{TOT}{}^2 + \Delta(\widetilde{N}_B + \widetilde{N}_D)^2)^{1/2} \tag{5}$$

$$\Delta N_S \approx \Delta N_{TOT} = (N_{TOT})^{1/2} \tag{6}$$

$$\Delta N_S/Ns = (1/Ns + (N_B + N_D)/Ns^2)^{1/2} \tag{7}$$

For example, if $N_S = 100$ and $N_B + N_D = 0$, $\boldsymbol{\Delta N_S/N_S} = 0.1$, while for $N_S = 100$ and $N_B + N_D = 100$, $\boldsymbol{\Delta N_S/N_S} = 0.14$. As the background and dark signal, $N_B + N_D$, remains constant with altitude and the signal, N_S, decreases exponentially with altitude, the uncertainty in the photon counts increases with altitude.

4. Density and Temperature Calculations

The raw photon count profiles are combined in time and altitude, the background is subtracted, and the raw photon counts are corrected for range scaling and extinction. We follow the established methods, calculate the combined background and average dark photon count signal at 190-195 km and correcting the photon count profiles for extinction (Wang, 2003). The corrected photon count is used to deduce the shape of the density profile using Equation 2.1a and standard lidar standard inversion techniques (e.g. Leblanc et al., 1998; Wang, 2003; Cutler, 2001). The density profile is smoothed by 2 km (i.e., 41 range bins) and normalized at the lowest altitude, typically 40 km, to yield a relative density profile (Whiteman et al., 1992),

$$\frac{\rho(z_1)}{\rho(z_2)} = \frac{Ns(z_1)}{Ns(z_2)} \times \left(\frac{z_1}{z_2}\right)^2 \tag{8}$$

where ρ is the atmospheric density. The density profile of the three channels for October 18, 2018, is shown in Figure 3. While the profiles show the same behavior and similar features in altitude, the difference between the profiles grows with altitude. The ratio of densities between the three channels is shown in Figure 3. Over the whole altitude range the signals differ by about 10% with a systematic change over altitude.

The determination of the temperature profile from the atmospheric density profile (Irving, 2012) assumes both the hydrostatic approximation (Equation 9) and Ideal Gas Law (Equation 10),

$$\frac{\partial p(z)}{\partial z} = -\rho(z)g(z) \tag{9}$$

$$p(z) = \frac{\rho(z)RT}{M} \tag{10}$$

where g is the acceleration of gravity (9.8228 m s^{-2} at Chatanika (Thurairajah, 2009), p is the atmospheric pressure, ρ is the atmospheric density (kg/m^3), R is the ideal gas constant (8.3145 J K^{-1} mol^{-1}), T is the temperature (K), and M is the mean molecular weight of air (kg/mol), where dry air is assumed to be a uniform mixture of O_2, N_2, CO_2, etc. (2.8964×10^{-2} kg/mol). Departures from hydrostatic balance are only necessary to consider during intense small-scale systems (e.g., tornadoes or squall lines that occur in the troposphere) (e.g. Holton, 2004). This method assumes that the air is essentially dry and negligible amounts of water vapor are present in the stratosphere and mesosphere. These assumptions are be invalid in the presence of aerosols, polar stratospheric clouds, or noctilucent clouds (e.g., Stevens et al., 2003; 2005; Kelley et al., 2010, Collins et al., 2021).

 doi:10.20944/preprints202603.0047.v1

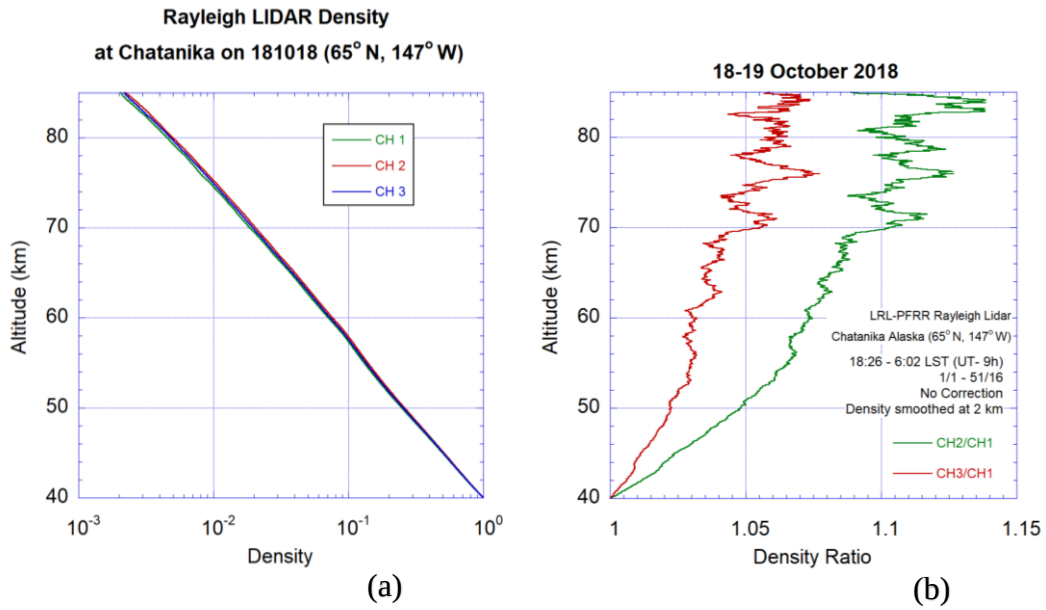

Figure 3. (a) Normalized atmospheric density profiles plotted as a function of altitude. The density profiles are each normalized to one at 40 km. Profiles are retrieved from the raw lidar signal profile measured on 18-19 October 2018 by RDTL (b) Ratio of Channel 2 and Channel 3 to Channel 1 density profiles plotted as a function of altitude.

Under the assumption that the atmosphere is in hydrostatic equilibrium (Equation 9), and that the atmosphere is homogeneous and behaves as a uniform gas. Using the ideal gas law (Equation 10) as the equation of state, the atmospheric pressure is given by,

$$p(z_0) = p(z) - \int_z^{z_0} \rho(r)g(r)\,dr = \frac{R}{M}\rho(z_0)T(z_0) \tag{11}$$

where z_0 is an upper altitude and z is a lower altitude. The equation yields the following expression for the temperature,

$$T(z) = T(z0)\frac{\rho(z0)}{\rho(z)} + \frac{M}{R}\int_z^{z_0}\frac{\rho(r)}{\rho(z)}g(r)\,dr \tag{12}$$

The temperature is initialized at an upper altitude (z_0, e.g., 85 km) using a climatology or local measurement (e.g., MSIS or SPARC). In the downward integration, from lower density at z_0 to higher density at z, the ratio $\rho(z_0)/\rho(z)$ decreases and the temperature estimate is increasingly less sensitive to the initial temperature and any error associated with it. Substituting the ratio of the range-scaled lidar signal for the ratio of the atmospheric densities we obtain,

$$T(z) = T(z_0)\frac{N(Z_0)}{N(Z)}\left(\frac{z_0}{z}\right)^2 + \frac{M}{R}\int_z^{z0}\frac{N(r)}{N(z)}\left(\frac{r}{z}\right)^2 g(r)dr \tag{13}$$

Due to the data acquisition method, the lidar profile is a series of discrete values. The downward integration method becomes a summation of the 48 m range bins. The lowest altitude of temperature retrieval is chosen at 40 km to ensure no contamination from aerosols, and the count rate does not exceed the maximum determined by the system detector. The temperature profile for 18-19 October 2018 is shown in Figure 4. Figure 4 and Table 3 show a significant difference in temperatures between the three channels in altitudes from 40-80 km. The differences in the individual density profiles (Figure 3) leads to the difference in their temperatures. In Figure 3 we see that Channel 2 and Channel 3 density profiles decrease less rapidly with altitude than Channel 1 as the ratios increase. This bias results in Channel 2 and Channel 3 measurements reflecting a warmer atmosphere than Channel 1, as in a warmer atmosphere the density decreases more gradually with altitude and has a larger scale height. This is indeed what we see in the temperature profiles in Figure 4. While all the temperature profiles show similar local maxima and minima, with a stratopause at 53 km, the temperatures retrieved from Channel 2 and Chanel 3 have higher values than those retrieved from Channel 1 by

 doi:10.20944/preprints202603.0047.v1

up to 8 K. The differences decrease as altitude increases reflecting the fact that the ratio between the signals changes most at the lower altitudes between 40 and 60 km.

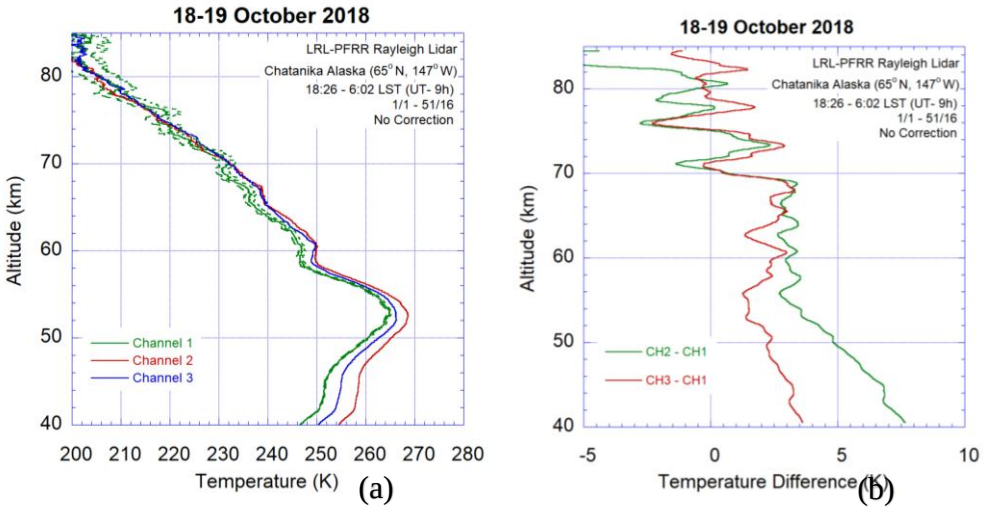

Figure 4. (a) The temperature profiles plotted as a function of altitude, measured by the RDTL on 18-19 October 2018 based on uncorrected lidar signals. (b) Difference in temperatures between Channel 1 and both Channel 2 and Channel 3 plotted as a function of altitude.

Table 3. Differences in temperatures between channels on October 18-19, 2018, based on uncorrected lidar signals.

Altitude (km)	$T_2 - T_1$ (K)	$T_3 - T_1$ (K)	ΔT_1 (K)	ΔT_2 (K)	ΔT_3 (K)
40	7.98	3.77	0.12	0.09	0.08
45	6.90	3.27	0.22	0.18	0.17
50	4.79	2.18	0.38	0.31	0.30
55	3.03	1.45	0.64	0.55	0.54
60	2.84	2.39	1.05	0.94	0.94
70	0.57	0.21	3.54	3.30	3.35
75	0.11	1.17	6.97	6.58	6.68
80	0.78	0.59	13.93	13.47	13.65

Given that the difference between the signals is most pronounced at the lower altitudes where the signals are greatest, Channel 2 and Channel 3 are distorted relative to Channel 1. We consider three sources of distortion in the signals. These are (i) pulse pile-up where photons arrive close in time and the PMT cannot discriminate between them, they are counted as a single broad pulse and the data acquisition system under counts the signals, (ii) variation in the detector gain due to the gain switching of the PMT, and (iii) variations in gain due to the amplitude of signal.

5. Pulse Pile-Up

The lidar photon counting signals are statistical and behave like Poisson random variables. Poisson's Theorem gives the probability distribution P of measuring k counts in a time interval τ_d (e.g., Papoulis, 1984; Taylor, 1996) as,

 doi:10.20944/preprints202603.0047.v1

$$P\{k \text{ in } \tau_d\} = e^{-x}\,\frac{x^k}{k!} \tag{14}$$

where $x = C \times \tau_d$ is the expected number of counts in τ_d and C is the mean count rate or number of counts per unit time. P must satisfy,

$$\sum_{i=0}^{\infty} P\{i\} = 1 \tag{15}$$

Pulse overlap occurs if the pulses have a finite nonzero width, in the case of photomultiplier tubes (PMTs) ~5 ns. If a pulse arrives and a subsequent pulse arrives within 5 ns then the two pulses will overlap and appear as a single pulse. Thus, the two pulses have "piled up". For the correction of pulse pile-up in RDTL, we use a pulse width of 9 ns. When pulse pile-up does not occur, we have a linear relationship between the optical and electrical signals from the receiver. When pulses overlap, or pile-up does occur, we have a nonlinear relationship. As signal levels increase, the pulses pile-up more often and the nonlinear effects increase (Irving, 2012). For Rayleigh lidar which is a non-paralyzable system, the detector is unresponsive to incoming pulses for a time interval τ_d after a pulse arrives. If a pulse arrives during that interval τ_d the pulse is ignored but the interval is not extended. Thus, a pulse arriving τ_d after an initial pulse is detected regardless of whether any pulses arrive in the intervening τ_d. Thus, the non-paralyzable detector cannot be paralyzed by succeeding pulses. The observed counting rate for a non-paralyzable system, C_{OBS} is given in terms of the true count rate, C_{TRUE}, as,

$$C_{OBS} = c_{TRUE}/(1 + x_{TRUE}) \tag{16}$$

And so,

$$C_{OBS} = c_{TRUE}/(1 + x_{TRUE}) \tag{17}$$

where $x_{TRUE} = C_{TRUE} \times \tau_d$, and $x_{OBS} = C_{OBS} \times \tau_d$. To correct the pulse pile-up in the 3-channel Rayleigh lidar, the data is binned in 15 minutes in time and smoothed over 2 kilometers (~42 range bins) in altitude in order to increase the confidence in the data. The observed count rate is determined by the total signal over 15 minutes,

$$C_{OBS} = \frac{N_{OBS}}{(\Delta t \times RL)(2\Delta z/c)} \tag{18}$$

where N_{OBS} is the total lidar signal (including signal, background, and dark signals), R_L is pulse repetition rate (= 20 pps), Δt (= 900 s) and Δz (= 48 m) are the temporal and spatial resolution of the signal, and c is the speed of light. The count rate is determined on a per laser pulse basis, $N_{TOT}/((2\Delta z/c) \times (\Delta t \times R_L)$ where N_{TOT} is the total signal per laser pulse, $2\Delta z/c$ is the time interval corresponding to an individual range bin, and $\Delta t \times R_L$ is the total number of laser pulses. The correction is then applied to the lidar signal as,

$$N_{TRUE} = N_{OBS}/(1 - x_{OBS}) \tag{19}$$

The choice of 15 minutes is to allow for a short enough interval to track signal variations due to energy changes in the laser and sky transmission, while providing enough signal to provide a statistically robust estimate of C_{OBS}. The density profiles and the ratio of the density profiles are plotted in Figure 5. Again, the density profiles are in general good agreement while the ratio of the density profiles is now reduced compared to the uncorrected data. The value of the Channel 2 (Channel 3) to Channel 1 ratio is reduced to 1.04 (1.01) at 40 km from 1.05 (1.02). The difference in the values of temperature is now reduced. The temperature profiles and the difference in the temperature profiles are plotted in Figure 6. At 40 km the difference between the temperatures retrieved from Channel 1 and Channel 2 decreases from 7.98 K to 6.90 K and the difference between those from Channel 1 and Channel 3 decreases from 3.77 K to 2.30 K (Table 4). The amount of the correction

 doi:10.20944/preprints202603.0047.v1

decreases with altitude as the effect of pulse pile-up decreases as the signal levels decrease with altitude.

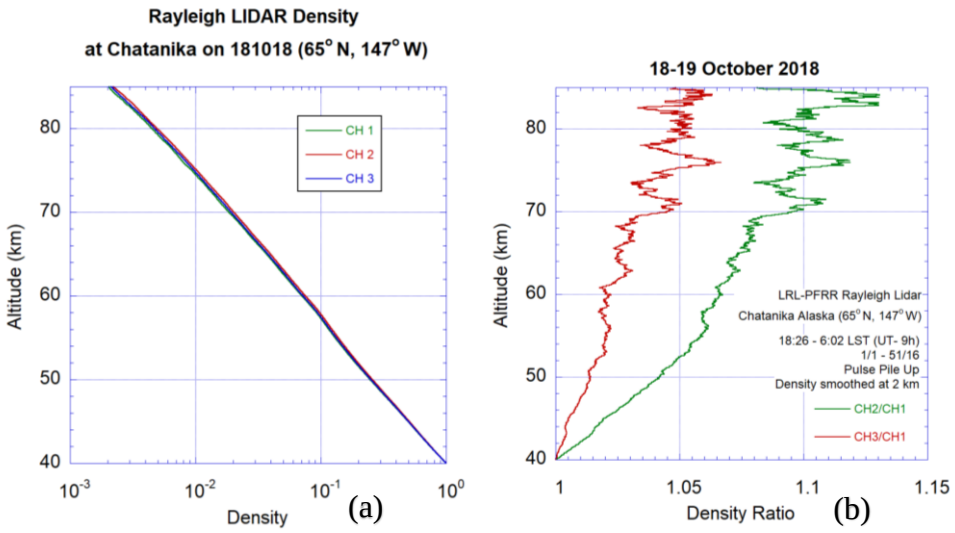

Figure 5. (a) Atmospheric density profiles plotted as a function of altitude. Each profile is normalized to one at 40 km. Profiles are retrieved from total lidar signal profile measured on 18-19 October 2018 and corrected for pulse pile-up. (b) Density ratio profiles plotted as a function of altitude measured on 18-19 October 2018 by the PFRR-RDTL after pulse pile-up correction.

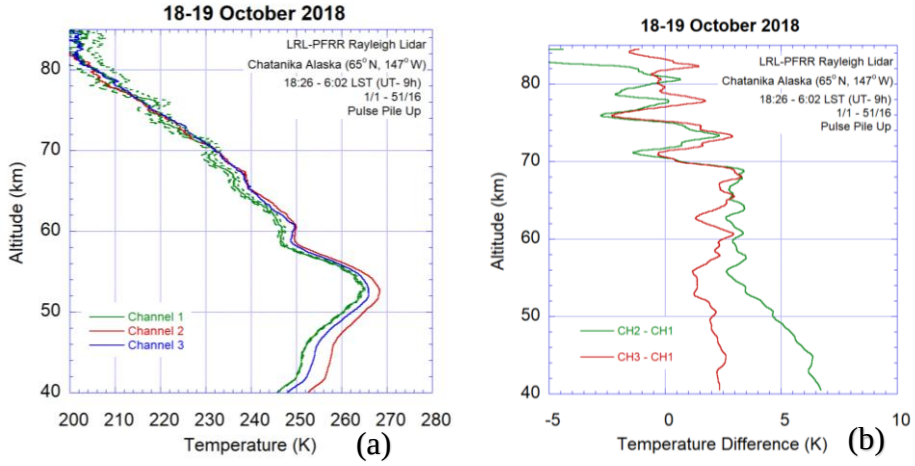

Figure 6. (a) The temperature profile plotted as a function of altitude, measured by the RDTL on 18-19 October 2018 after pulse pile-up correction. (b) Temperature difference profile plotted as a function of altitude, measured by the RDTL on 18-19 October 2018 after pulse pile-up correction.

Table 4. Lidar temperature differences between Channel 2 and 3 and Channel 1 on October 18, 2018, after correction for pulse pile-up.

Altitude (km)	$T_2 - T_1$ (K)	$T_3 - T_1$ (K)	ΔT_1 (K)	ΔT_2 (K)	ΔT_3 (K)
40	6.90	2.30	0.12	0.09	0.08
45	6.47	2.70	0.22	0.18	0.17
50	4.61	1.94	0.38	0.31	0.30
55	2.95	1.34	0.64	0.55	0.53

 doi:10.20944/preprints202603.0047.v1

60	2.81	2.34	1.05	0.94	0.93
70	0.56	0.2	3.53	3.31	3.35
75	0.11	1.17	6.92	6.54	6.39
80	0.78	0.59	13.93	13.47	13.65

6. Detector Gain Switching

The RDTL gain switches the PMTs by controlling the voltage between the photocathode and the first dynode of the PMT. The photocathode is at a voltage of -2000V and the anode is at 0 V. A voltage of 200 V is applied to the first dynode of the PMT to reduce the voltage between the photocathode and the first dynode, and thus reduce the acceleration of electrons through the PMT and the gain of the PMT. As mentioned earlier, the application of the 200V signal is triggered by the laser Q-switch, so that the gain switching commences just before the laser pulse is transmitted. The return signals from altitudes below a selected altitude are thus detected at low gain while higher-altitude signals are detected at high gain. The lidar uses switching of the electric bias of the PMT to eliminate the signal coming from the lower altitudes.

A test was performed where the lidar receiver system was exposed to different intensities of light using fluorescent light bulbs that were placed in the telescope. The data acquisition system was triggered with a signal generator. The test enabled us to test the receiver system and the effects of the gain switching. The signal mimics a skylight signal that is constant with altitude. Figure 7 shows Channel 1 signal with altitude. The test of the three channels revealed an exponential variation of signal in each of the three channels that can be expressed in the form of following equation,

$$N_g(z) = A + B\,(1 - e^{-(z-z_0)/\lambda}) \quad \text{for } z > z_0 \tag{20}$$

where $N_g(z)$ is the signal obtained from light bulbs. A, B and λ are channel specific constants and z_o is the corresponding switching or blanking altitude. Ideally, we would expect $N_g(z) = N_0$, a constant value for $z > z_0$. Ideally, the count remains constant with height, however, the fitted curve represents the actual signal showing the recovery from gain switching. The gain of the PMT is now calculated as,

$$g(z) = Ng(z)/\,N_0 \text{ for } z > z_0 \tag{21}$$

where $g(z) = 1$ as $z \rightarrow \infty$, and so,

$$g(z) = \frac{A + B\left(1 - e^{-\frac{(z-z_0)}{\lambda}}\right)}{A+B} \quad \text{for } z > z_0 \tag{22}$$

Thus, we correct the lidar signals for PMT gain switching by dividing the signals that have been corrected for pulse pile-up by g(z). The value of the fitted constants and z_0 for the three channels is listed in Table 5. Figure 8 and Figure 9 show the changes in density and temperature with altitude between the three channels after corrections for pulse pile-up and blanking response are applied to the lidar data. Again, we see that the density profiles from the three channels have the same general features with altitude, and the ratio of the different channels further decreases. The differences in the temperature profiles also decrease (Table 6). At 40 km the difference between the temperatures retrieved from Channel 1 and Channel 2 decreases from 6.90 K to 6.60 K and the difference between those from Channel 1 and Channel 3 decreases from 2.30 K to 1.53 K (Table 4). The amount of the correction decreases with altitude as the value of g(z) approaches 1.

Preprints.org (www.preprints.org) | NOT PEER-REVIEWED | Posted: 2 March 2026 doi:10.20944/preprints202603.0047.v1

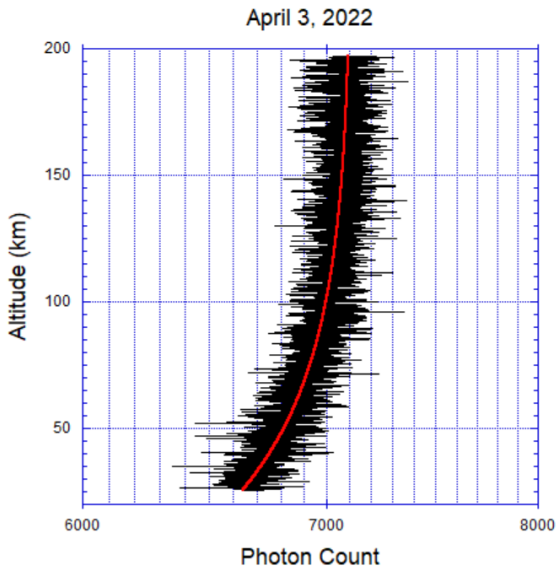

Figure 7. Channel 1 lidar signal plotted with altitude on April 3, 2022. The red curve is the fitted curve.

Table 5. Channel constants for the 3 channel Rayleigh system.

Constant	Channel 1	Channel 2	Channel 3
A	217832	112558	141465
B	14698.3	5507.6	11355.0
λ (km)	58	38	49
z_0 (km)	25.49	32.25	32.30

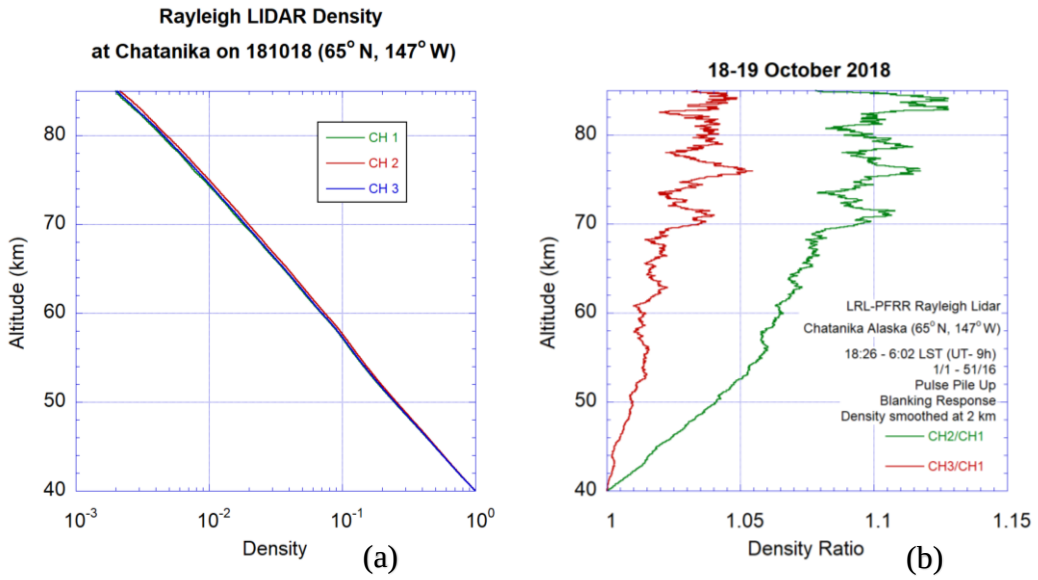

Figure 8. (a) Atmospheric density profile plotted as a function of altitude retrieved from the total photon count profile measured on 18-19 October 2018 by the PFRR-RDTL and normalized to one at 40 km after pulse pile-up and PMT gain switching response. (b) Density ratio profile plotted as a function of altitude measured on 18-19 October 2018 by the RDTL after pulse pile-up and detector gain-switching correction.

 doi:10.20944/preprints202603.0047.v1

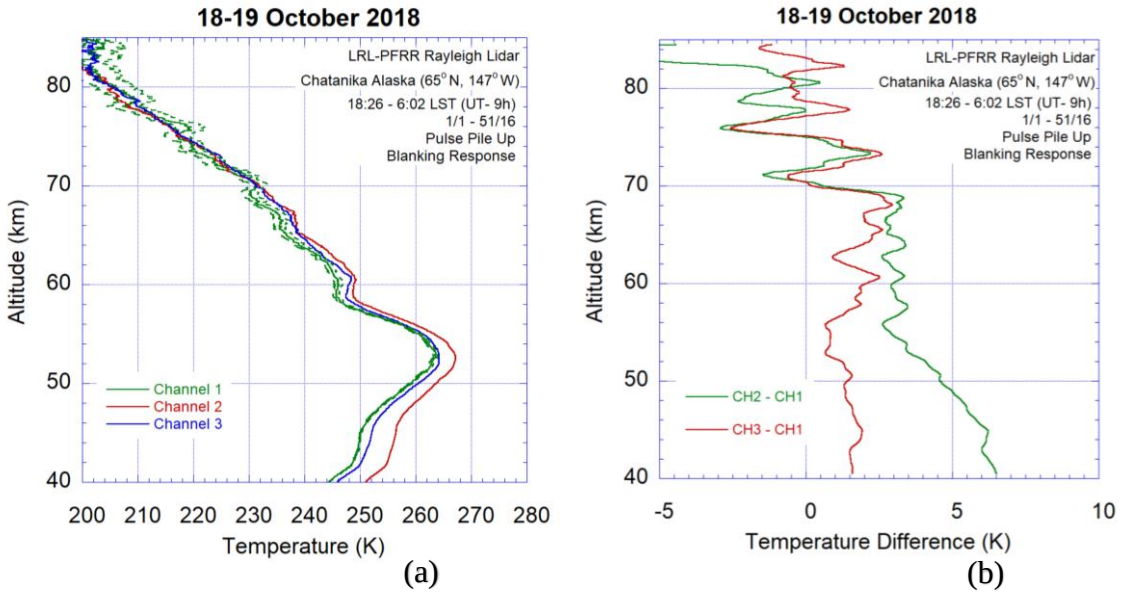

Figure 9. (a) The temperature profile plotted as a function of altitude, measured by the PFRR-RDTL on 18-19 October 2018 after correction for pulse pile-up and PMT gain switching. (b) Temperature difference profile plotted as a function of altitude, measured by the PFRR-RDTL on 18-19 October 2018 after correction for pulse pile-up and PMT gain switching channels after the signals have been corrected for pulse pile-up and PMT gain switching.

Table 6. Lidar temperatures on October 18, 2018, after correction for pulse pile-up and PMT gain switching.

Altitude (km)	$T_2 - T_1$ (K)	$T_3 - T_1$ (K)	ΔT_1 (K)	ΔT_2 (K)	ΔT_3 (K)
40	6.60	1.53	0.12	0.09	0.08
45	6.33	1.99	0.20	0.15	0.14
50	4.53	1.31	0.33	0.26	0.24
55	2.93	0.81	0.54	0.44	0.42
60	2.78	1.89	0.85	0.74	0.71
70	0.49	0.12	2.65	2.51	2.46
75	-0.03	0.89	5.08	4.92	4.85
80	0.60	0.38	10.07	10.03	9.87

7. Signal Amplitude

The final correction assumes that the shape of the Channel 1 signal reproduces the atmospheric density profile most faithfully. This is based on the fact that Channel 1 signals have the lowest amplitude and therefore are least susceptible to changes in gain due to variations in the power supply terminal voltage. Thus, the Channel 1 signal is taken as the reference for Channel 2 and Channel 3 signal. The correction is implemented as a ratio correction. The temperature and density profiles are first calculated for each of the channels. The temperature profiles from Channel 2 and Channel 3 are compared with those of Channel 1. Starting either at the top of the profiles, the profiles are compared moving downward until the amplitude where the difference between the temperatures becomes greater than the uncertainties in the difference between the profiles,

 doi:10.20944/preprints202603.0047.v1

$$(T_1(z) - T_{2,3}(z))^2 > (\Delta T_1(z))^2 + (\Delta T_{2,3}(z))^2 \text{ for } z < z_{S2,3} \quad (21)$$

where ΔT_i is the statistical uncertainty in the temperature moving upward from the bottom of the profiles to the altitude to where the difference between the temperatures becomes less than the uncertainties in the difference between the profiles,

$$(T_1(z) - T_{2,3}(z))^2 < (\Delta T_1(z))^2 + (\Delta T_{2,3}(z))^2 \text{ for } z > z_{S2,3} \quad (22)$$

Once $z_{S2,3}$ is calculated we now take the ratio of the Channel 1 density profile to the Channel 2 and Channel 3 density profiles. This ratio is calculated as follows,

$$R_{2,3}(z) = \frac{\rho_1(z)}{\rho_1(z_{S2,3})} \times \frac{\rho_{2,3}(zS2,3)}{\rho_{2,3}(z)} \quad [z < z_{S2,3}] \quad (23)$$

$$R_{2,3}(z) = 1 \; [z > z_{S2,3}] \quad (24)$$

In this correction method, the temperatures and uncertainty in temperatures are first calculated of the individual channels from selected altitude range (e.g., 38 to 85 km) after correcting the total signal for pulse pile-up and blanking response. The individual channel temperatures are then smoothed, and a difference is taken between Channel 1 and the Channel for which the factor is being calculated (e.g. Channel 2). A reference altitude is then calculated where the temperature difference between the two channels is still greater than the total error from the two channels. Let this altitude be $z_{S1,2}$ and the temperatures are similar between the two compared channels beyond this altitude.

The ratios between Channel 1 and Channel 3 are also calculated in the same way up to $z_{s1,3.}$ For October 18, 2018, the value of z_s for Channels 2 and 3 are 69.3 km and 69.1 km respectively. Figure 10 shows the ratio correction curve for channel 2 on October 18, 2018. The background signal is removed and the lidar signal count is then corrected for the ratio correction using,

$$N_{2s}(z) = N_{2s}(z) \times R_{1,2}(z) \quad (25)$$

$$N_{3s}(z) = N_{3s}(z) \times R_{1,3}(z) \quad (26)$$

where N_s is the signal component. The background skylight count is then calculated for the individual channels and is added to the signal. The background signal is the mean signal from 187.5 to 192.5 km. The background signal is then added for all three channels and is used to calculate the combined densities and temperatures profiles.

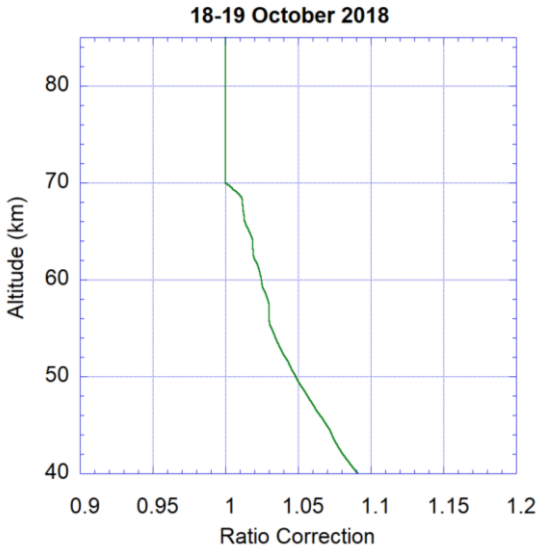

Figure 10. Ratio for signal amplitude correction curve for channel 2 plotted as a function of altitude.

 doi:10.20944/preprints202603.0047.v1

Figures 11 and 12 show the change in density and temperature with altitude after corrections for pulse pile-up, blanking response, and ratio are applied to the data. The density and temperature profiles from the three channels are in good agreement with each other over the whole altitude range. The deviation in temperatures between the three channels is less than 0.05% in all altitudes. As the noise increases above 70 km, the difference in the temperature measurements between the three channels increases beyond 70 km (Table 7). The density and temperature profile derived after combining all three channels together also shows good agreement with the individual channel density and temperature (Figures 13 and 14).

Table 7. Lidar temperatures on October 18, 2018, after corrections for pulse pile-up, detector gain-switching, and ratio.

Altitude (km)	$T_2 - T_1$ (K)	$T_3 - T_1$ (K)	ΔT_1 (K)	ΔT_2 (K)	ΔT_3 (K)	$\Delta T_{combined}$ (K)
40	-0.01	-0.02	0.11	0.08	0.08	0.06
45	0.29	0.2	0.22	0.17	0.16	0.14
50	0.03	0.05	0.37	0.30	0.29	0.26
55	0.37	0.37	0.63	0.53	0.52	0.48
60	0.37	0.39	1.04	0.92	0.91	0.86
70	0.49	0.12	3.52	3.29	3.33	3.26
75	-0.03	0.89	6.94	6.56	6.65	6.57
80	0.60	0.38	13.92	13.45	13.63	13.49

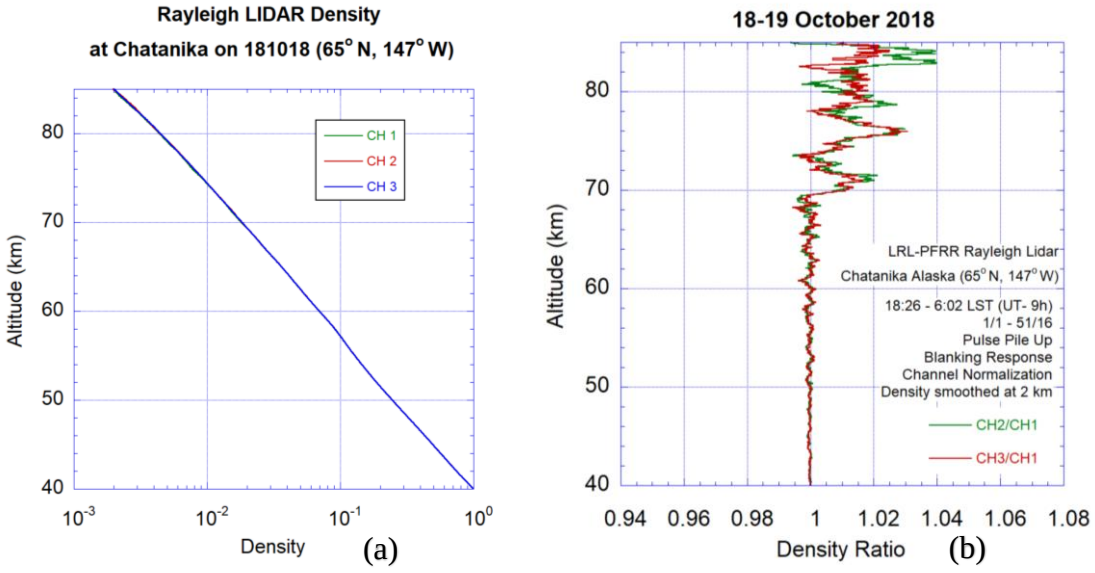

Figure 11. (a) Atmospheric density in relative units (RU) plotted as a function of altitude retrieved from the total photon count profile measured on 18-19 October 2018 by the PFRR-RDTL. Density is normalized to one at 40 km after pulse pile-up, detector gain-switching response, and signal amplitude correction. (b) Atmospheric density ratio plotted as a function of altitude measured on 18-19 October 2018 by the PFRR-RDTL after pulse pile-up, detector gain-switching response, and signal amplitude correction.

 doi:10.20944/preprints202603.0047.v1

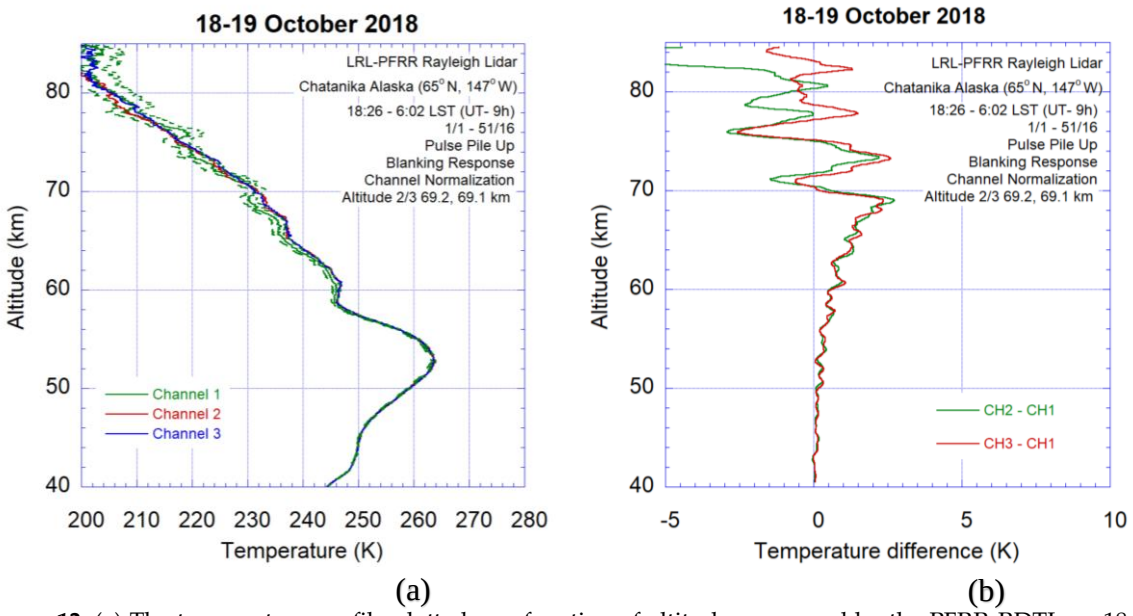

Figure 12. (a) The temperature profile plotted as a function of altitude, measured by the PFRR-RDTL on 18-19 October 2018 after correction for pulse pile-up, blanking response, and signal amplitude correction. (b) Temperature difference profile plotted as a function of altitude, measured by the PFRR-RDTL on 18-19 October 2018 after pulse pile-up, blanking response, and signal amplitude correction.

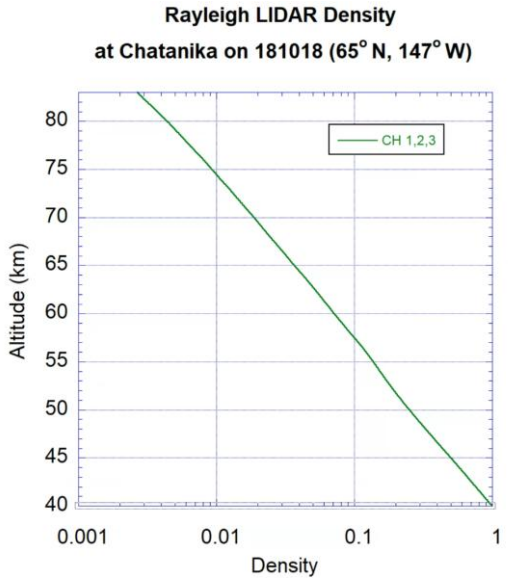

Figure 13. Atmospheric density profile plotted as a function of altitude retrieved from the total photon count profile measured on 18-19 October 2018 by the PFRR-RDTL and normalized to one at 40 km after combining all three channels.

 doi:10.20944/preprints202603.0047.v1

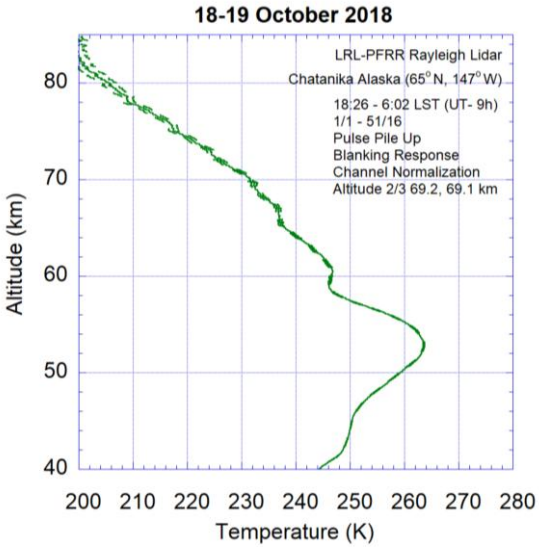

Figure 14. The temperature profile ± uncertainties plotted as a function of altitude, measured by the PFRR-RDTL on 18-19 October 2018 after combining all three channels.

Table 8 summarizes the temperatures from different channels at selected altitudes after each correction is applied to the data. As expected, the correction due to pulse pile-up is more significant at the lower altitudes. The temperatures between the three channels converge after all the corrections are applied.

Table 8. Lidar temperatures on October 18, 2018, at different altitude.

Correction	40 km	45 km	50 km	55 km	60 km
No Correction					
Channel 1	246.6 K	251.8 K	260.5 K	261.5 K	246.9 K
Channel 2	254.6 K	258.7 K	265.3 K	264.5 K	249.8 K
Channel 3	250.4 K	255.1 K	262.7 K	262.9 K	249.4 K
Pulse Pile-Up					
Channel 1	245.8 K	251.5 K	260.4 K	261.4 K	246.9 K
Channel 2	252.7 K	257.9 K	264.9 K	264.4 K	249.8 K
Channel 3	248.1 K	254.2 K	262.3 K	262.8 K	249.3 K
Pulse Pile-Up and Gain Switching					
Pulse Pile-Up, Gain Switching, and Signal Amplitude					
Channel 1	244.5 K	250.1 K	259.1 K	260.4 K	246.1 K
Channel 2	244.4 K	250.4 K	259.1 K	260.7 K	246.5 K
Channel 3	244.3 K	250.3 K	259.2 K	260.7 K	246.5 K

8. Conclusions

A new 3-channel correction procedure has been developed and deployed to the data processing technique of a Rayleigh lidar installed at Poker Flat Research Range (PFRR), Chatanika, Alaska.

 doi:10.20944/preprints202603.0047.v1

Temperature measurements from the individual channels showed a disagreement in temperatures especially in the lower altitudes and hence the need of the correction procedure that ensures better agreement of temperatures between the three channels. The major conclusions from the study are as follows.

1) Due to the effect of pulse pile-up, underestimation of signal leads to warmer atmosphere in the lower altitudes. As, channel 2, and 3 has higher signal counts than channel 1, these channels have higher effect of pulse-pile up. We achieve 38% better agreement in temperatures at 40 km after the correction of pulse pile-up.
2) The electronic blanking produces an instrumental bias in the signal which leads to warmer temperatures as well. The nature of the bias is similar for all three channels and decreases with increasing altitude. Once the data is corrected for the bias caused by gain switching and pulse pile-up, we get 60% better agreement in temperatures at 40 km.
3) As, channels 2 and 3 gets almost twice the signal compared to channel 1, the accelerated electrons in the photomultiplier tube for these two bumps into each other and create a bias in the photon calculations. Once channels 2 and 3 are corrected for the signal amplitude, we get 99.4% agreement in temperatures at 40 km.

In summary, the 3-Channel correction reduces instrumental bias in the Rayleigh lidar data and once the individual channel signals are combined into one; the resulting signal counts yield accurate measurements of the temperatures. As, the procedure is implemented in the data acquisition process, it can be used to other lidar data as well to reduce instrumental bias significantly.

Author Contributions: Conceptualization, R.C.; methodology, R.C. and S.D.; software, R.C. and S.D..; validation, S.D., R.C. and J.L.; formal analysis, S.D..; investigation, R.C., S.D. and J.L.; resources, R.C., S.D., and J.L.; data curation, S.D. and J.L.; writing—original draft preparation, S.D.; writing—review and editing, S.D., and R.C.; visualization, R.C. and S.D.; supervision, R.C.; project administration, R.C. and J.L.; funding acquisition, R.C. All authors have read and agreed to the published version of the manuscript.

Data Availability Statement: The Rayleigh lidar data used for the study is available at https://data.mendeley.com/datasets/fsmcntshw3/1.

Acknowledgments: This study was supported by the National Science Foundation (NSF) and National Aeronautics and Space Administration (NASA) under the following grants and contracts: NASA 80NSSC21K000, NSF 1651463, NSF 1829161, and NSF 2048628. The authors also thank the staff at Poker Flat Research Range for operating and maintaining the range facilities.

Conflicts of Interest: The funders had no role in the design of the study; in the collection, analyses, or interpretation of data; in the writing of the manuscript; or in the decision to publish the results.

References

1. Mizutani, K.; Itabe, T.; Yasui, M.; Aoki, T.; Murayama, Y.; Collins, R.L. Rayleigh and Rayleigh Doppler Lidars for the Observations of the Arctic Middle Atmosphere. *IEICE Transactions on Communications* **2000**, E83-B, 9, 2004-2009.
2. Cutler, L. J.; Collins, R.L.; Mizutani, K.; Itabe, T. Rayleigh lidar observations of mesospheric inversion layers at Poker Flat, Alaska (65^{0}N, 147^{0}W). *Geophys. Res. Lett.* **2001**, 28(8), 1467–1470.
3. Collins, R.L.; Kelley, M.C.; Nicolls, M. J.; Ramos, C.; Hou, T.; Stern, T. E.; Mizutani, K.; Itabe, T. Simultaneous lidar observations of a noctilucent cloud and an internal wave in the polar mesosphere. *J. Geophys. Res*. **2003,** 108(D8), 8435.
4. Triplett, C. C.; Li, J.; Collins, R. L.; Lehmacher, G. A.; Barjatya, A.; Fritts, D.C. Observations of reducedturbulence and wave activity in theArctic middle atmosphere following the January 2015 sudden stratospheric warming. *Journal of Geophysical Research: Atmospheres* **2018**, 123,13,259-13,276.
5. Alspach, J. H. Lidar and satellite studies of Noctilucent clouds over Alaska. M.S. Thesis, University of Alaska, Fairbanks, 2020.

 doi:10.20944/preprints202603.0047.v1

6. Papoulis, A.; Pillai, S. U. *Probability, random variables and stochastic processes,* Mc Graw Hill: New York, United States, 2002; pp852.
7. Wang, W. Spectral estimation of signal and noise power in Rayleigh lidar measurements of the middle atmosphere. M.S. Thesis, University of Alaska, Fairbanks, 2003.
8. Leblanc, T.; McDermid, I. S.; Hauchecorne, A.; Keckhut, P. Evaluation of optimization of lidar temperature analysis algorithms using simulated data. *J. Geophys. Res*. **1998**, 103, 6177–6187.
9. Whiteman, D. N.; Melfi, S. H.; Ferrare, R. A. Raman lidar system for the measurement of water vapor and aerosols in the Earth's atmosphere. *Applied Optics* ***1992***, *31*, 3068–3082.
10. Irving, B. K. Rayleigh lidar studies of mesospheric inversion layers at Poker Flat Research Range, Chatanika, Alaska. M.S. Thesis, University of Alaska, Fairbanks, 2012.
11. Thurairajah, B.; Collins, R.L.; Mizutani, K. Multi-year temperature measurements of the middle atmosphere at Chatanika, Alaska (65°N, 147°W). *Earth Planets Space* **2009,** 61(6), 755–764.
12. Holton, J. R. *An Introduction to Dynamic Meteorology*, Elsevier Acad. Press: Massachusetts, United States, 2004; pp535.
13. Stevens, M. H.; Englert, C. R.; DeLand, M. T.; Hervig, M. Polar mesospheric clouds formed from space shuttle exhaust. *Geophysical Research Letters* ***2003***, 30(10), 1546.
14. Stevens, M. H.; Meier, R. R.; Chu, X.; DeLand, M. T.; Plane, J. M. C. Antarctic mesospheric clouds formed from space shuttle exhaust. *Geophysical Research Letters* ***2005***, 32(13), L13810.
15. Kelley, M. C.; Nicolls, M. J.; Varney, R. H.; Collins, R. L.; Doe, R.; Plane, J. M. C.; Thayer, J.; Taylor, M.; Thurairajah, B.; Mizutani, K. Radar, lidar, and optical observations in the polar summer mesosphere shortly after a space shuttle launch. *Journal of Geophysical Research: Space Physics 2010,* 115(A5), A05304.
16. Collins, R. L.; Stevens, M. H.; Azeem, I.; Taylor, M. J.; Larsen, M. F.; Williams, B. P.; Li, J.; Alspach, J. H.; Pautet, P. D.; Zhao, Y.; Zhu, X. *Cloud Formation From a Localized Water Release in the Upper Mesosphere: Indication of Rapid Cooling. Journal of Geophysical Research: Space Physics* **2021**. 126(2), e2019JA027285.
17. Taylor, J. C. *An Introduction to Measure and Probability.* Springer: New York, United States, 1996; ISBN 978-0-387-94830-0.
18. Das, S. Three-Channel Rayleigh Lidar System Signal Retrievals. Mendeley Data V1 **2026**.